Materials Advances

Accepted Manuscript

This article can be cited before page numbers have been issued, to do this please use: M. U. Salman and S. Atiq, *Mater. Adv.*, 2025, DOI: 10.1039/D5MA01257K.

ROYAL SOCIETY OF CHEMISTRY

rsc.li/materials-advances

View Article Online
DOI: 10.1039/D5MA01257K

Optimization of lead-free $BiFeO_3$ perovskite solar cell for efficient solar potential in futuristic green technologies

Muhammad Umar Salman*, Shahid Atiq**

Centre of Excellence in Solid State Physics, University of the Punjab, Lahore-54590, Pakistan

Abstract

The adverse effects of global warming and dependence on hazardous energy sources like coal and petroleum have shifted focus toward solar energy, a sustainable and clean solution. Perovskite materials, particularly $BiFeO_3$, are attracting attention as absorber layers due to their multifunctional properties. This study employs COMSOL to simulate 1D TiO_2/$BiFeO_3$/Spiro-OMeTAD solar cell with ideal ohmic contacts at different operating temperatures. The results demonstrate that short-circuit current density increases with $BiFeO_3$ thickness, and efficiency peaks at an optimal thickness. However, the maximum efficiency of 10.88% is achieved (in TiO_2/$BiFeO_3$/Spiro-OMeTAD) when the electron transport layer has density of states in valence and conduction band (N_CN_V) ~ 2×10^{16} cm^{-3} while TiO_2/SnS/$BiFeO_3$/Spiro-OMeTAD showed maximum efficiency of 20.99% at 700 nm thickness of SnS layer. Moreover, an increase in $BiFeO_3$'s bandgap enhances the open-circuit voltage (V_{oc}) but reduces the fill factor. On the other hand, the $BiFeO_3$'s N_CN_V has no significant impact on efficiency but shows inverse coupling with V_{oc}. Additionally, increasing $BiFeO_3$'s electron affinity improves the fill factor, while TiO_2's electron affinity enhances V_{oc}, and that of Spiro improves power output. This work provides insights for optimizing material properties and device parameters in experimental applications and highlights the potential of $BiFeO_3$-based perovskite for next-generation photovoltaics.

Keywords: Green energy, Solar energy, COMSOL simulations; Perovskite solar cells; TiO_2; Spiro-OMeTAD;
Inverse coupling

Corresponding Author: *Muhammad Umar Salman (muhammadumarsalmanm@gmail.com); **Shahid Atiq (satiq.cssp@pu.edu.pk)

View Article Online
DOI: 10.1039/D5MA01257K

1. Introduction

The global energy crisis can be addressed by solar energy, which is a sustainable, non-polluting, and inexhaustible source of energy [1-3]. For this purpose, to this end, the extensively studied materials for photovoltaic (PV) applications are organic, inorganic or hybrid perovskite solar cells (PSCs). Since 2009, these PSCs have demonstrated robust improvement in power conversion efficiency (η), lifting from 3.8% to 26% approximately [4-6]. PSCs have been identified as next-generation PV technology, surpassing behind the conventional solar cell, however, the perovskites (PVKs) exhibiting strong ferroelectric (FE) response are particularly preferred [7]. Conventional solar cells are based on crystalline silicon (c-Si) technologies, that operate through a single p-n junction mechanism with fixed material interfaces and well-defined efficiency limits determined by the Shockley-Queisser limit. They rely on established material and design parameters and have long served as performance benchmarks for evaluating emerging solar technologies. The inherent spontaneous polarization of FE materials facilitates the separation of the photogenerated electron-hole pairs without developing the conventional n-type and p-type depletion region. There are many factors driving the PV nature of FE materials including Schottky barrier effect, bulk PV effect, domain wall theory, etc., [8-10]. Specifically, the alignment of domains within the FE material induces the polarization, which further produces the depolarization field. When the built-in field and depolarization field are aligned in the same direction, this alignment promotes efficient separation of electrons and holes [11]. The spontaneous polarization arises from the off-center & non-centrosymmetric displacement of positive and negative ions in ABO_3 structure of FE materials [12,13]. Various PVK materials have been reported so far, including $BaTiO_3$, $Bi_4Ti_3O_{12}$, and PZT [14-17]. But the key limitation associated with these materials is the larger band gap (E_g), often exceeding 3 eV, that isn't feasible to be practical for solar energy conversion under sunlight. This large E_g is resulted from the high electronegativity difference between *B*-site and oxygen atoms. Therefore, reducing the E_g is crucial to improve η of FE materials in PV applications. Hence, the band gap engineering through the substitution of appropriate metal cation at *B*-site can alter both FE response and E_g of FE materials. So, a completely new FE material for PV applications is needed, having both high induced polarization and a small E_g, and $BiFeO_3$ (BFO) emerges as the potential candidate, as it does not only fulfil these requirements but also non-toxic.

View Article Online
DOI: 10.1039/D5MA01257K

BFO, a multiferroic (rhombohedral symmetry, *R*3*c* space group) retains its multiferroicity above or at room temperature (RT), with a Curie temperature (T_C ~ 1103 K) and G-type antiferromagnetic Neel temperature (T_N ~ 643 K). BFO is widely employed in magneto-electric, optoelectronic devices, multistate memory devices, and spintronics devices, due to its quite high remnant polarization (~ 100 μC/cm^2) and that is sufficient to efficiently separate the photogenerated electron-hole pairs [18-23]. At RT, BFO is stable and exhibits both magnetic and electric responses spontaneously, with a lower direct/indirect E_g (2.1 – 2.8/ 1.07 eV) and high absorption coefficient (~ 10^5 cm^{-1} at 400 nm) [24-32]. The thin films of BFO exhibit the lower series resistance, which excels the enhanced collection of photogenerated charge carriers [33]. Notably, the switching of photocurrent is possible by simply switching the direction of spontaneous polarization. These properties render BFO a potential candidate among the other conventional PVK materials for better optical and FE purposes. Despite the large open circuit voltage (V_{oc}) but still BFO-based solar cells are facing the challenge of lower η than commercial Si-based cells. The highest experimentally reported η for BFO is 10% so far, though it can be improved by tuning the FE response and E_g [34, 35]. There may be many reasons for this low η but major limiting factors include high leakage currents and low magnetization, possible due to oxygen vacancies, high volatilization of Bi, valence fluctuations in Fe ions, or the presence of secondary phases [36-40]. These factors lead to η below its theoretical limits; however, BFO is the best choice of researchers because its ferroelectric and non-centrosymmetric nature enables polarization-driven charge separation through bulk and domain-wall photovoltaic effects [41,42]. Many strategies have been done to resolve these issues like conductivity, leakage current, and magnetization via substitution or composite [43,44]. However, these approaches often lead towards structural defects or secondary phases occurrence [45-49]. On parallel, researchers are trying hard to improve these factors via controlled synthesis process and insertion of electron transport layer (ETL) or hole transport layer (HTL) across BFO layer. Though effective, but these layers cause to create the interface defects and ultimately reduces the overall η of solar cell. Recently, HTL-free solar cells have been proposed, having fewer number of defects as well as lower in cost [50]. In BFO-based solar cells, TiO_2 has been widely employed as an ETL owing to its ease of synthesis, low cost, excellent crystalline stability, anisotropic growth behavior, and efficient electron transport characteristics [51].

View Article Online
DOI: 10.1039/D5MA01257K

The extensive study has been done from both experimental and theoretical groups such as, Kim *et al.* (2020), De Los *et al.* (2020), Karthick *et al.* (2020), Kumar *et al.* (2021), Sebastian *et al.* (2021), Singh *et al.* (2021) and Hossain *et al.* (2023) [52-58]. But no significant attention has been deployed to most advanced mathematical-based solver to simulate the BFO-based solar cell. In this study, we make use of most advanced COMSOL Multiphysics simulation software to simulate the 1D TiO_2/BFO/Spiro-OMeTAD heterojunction solar cell—a novel approach that has not been explored in past for enhancement of device performance. This software allows to vary multiple factors simultaneously, offering deep insights to improve η. The software is based on finite element method (FEM) which solves the Poisson's equation and drift-diffusion partial differential equations under the semiconduction physics. It allows to couple more than one physics simultaneously, enabling 3D simulation of complex devices. Based on advanced mathematical method, the accuracy of this software can be estimated by comparing the simulated output values, which normally show a difference of only 1.50% and 2.40% from the experimental data [59]. The sole purpose of this simulation-based study is to optimize the parameters efficiently, to improve the overall performance of cell. The better optimization of parameters leads towards the better output results of device and advanced tools of simulation give this opportunity. This includes the optimization of doping type, doping level, carrier concentration, defect type, defect density, thickness of layers, metal contacts etc. Once the parameters are optimized, then we simulate the solar cell to find out the output characteristics of solar cell, including current density-voltage (J-V) and power-voltage (P-V) curves for the determination of η and other quantities.

2. Numerical modeling

In this study, the COMSOL Multiphysics software was employed as a robust tool to analyze the underlying causes of low η in solar cells. Earlier investigations primarily utilized 1D or 2D simulation frameworks to study the basic characteristics of similar devices, the present work implements a 3D COMSOL-based model to capture realistic spatial effects and provide more accurate performance predictions. It forecasts the electrical behavior and internal physical mechanics of the structure as a physics-based 2D and 3D device simulator. It achieves this by solving fundamental equations, including Poisson's equation and carrier continuity equations, which establish a relationship between electrostatic potential and carrier densities [60]. For charge transport analysis, the Drift-Diffusion Model emerges as the most effective and computationally

View Article Online
DOI: 10.1039/D5MA01257K

efficient approach. Poisson's equation, which relates the electrostatic potential to the local space charge density, is expressed as (Eq. 1):

$$\nabla.(\varepsilon\nabla\psi) = -\rho \tag{1}$$

Here, ψ denotes the electrostatic potential, ε represents the local permittivity, and ρ signifies the local space charge density [61]. The steady-state continuity equations (Eq. 2,3) for electron and hole transport are described as follows:

$$\frac{\partial n}{\partial t} = \frac{1}{q}\nabla.\vec{J}_n + G_n + R_n \tag{2}$$

$$\frac{\partial p}{\partial t} = -\frac{1}{q}\nabla.\vec{J}_p + G_p + R_p \tag{3}$$

Here, $\vec{J}_n$ and $\vec{J}_p$ represent the current densities for electrons and holes, respectively, and the terms G_n and G_p denote the generation rates of charge carriers, while R_n and R_p represent the total recombination rates in Gaussian and tail states, whereas the electron charge is represented by q [62]. The term G, governing the rate of photogenerated electron-hole pairs, was incorporated in COMSOL to simulate light absorption across the active layer and is expressed $G = \alpha I_0 e^{-\alpha x}$. Here, α is the absorption coefficient, I_0 represents the incident light intensity, and x is the penetration depth. In the Drift-Diffusion Model, the current densities are related to the quasi-Fermi levels as (Eq. 4,5):

$$\vec{J}_n = -q\mu_n n\nabla\phi_n \tag{4}$$

$$\vec{J}_p = -q\mu_p p\nabla\phi_p \tag{5}$$

Here, μ_n and μ_p denote the mobilities of electrons and holes, respectively, while ϕ_n and ϕ_p represent the quasi-Fermi levels. Using the Boltzmann approximation, the quasi-Fermi levels are further linked to the electrostatic potential and carrier concentrations as (Eq. 6,7):

$$n = n_i \exp\left(\frac{\psi-\phi_n}{k_B T}\right) \tag{6}$$

$$p = n_i \exp\left(\frac{\psi-\phi_p}{k_B T}\right) \tag{7}$$

View Article Online
DOI: 10.1039/D5MA01257K

Here, T is the lattice temperature, k_B is the Boltzmann constant, and n_i represent the effective intrinsic carrier concentration [63]. The electrical properties of the device are computed based on the defined physical structure and applied bias conditions. This involves discretizing the governing equations (Poisson's equation and carrier continuity equations) over a finite element grid, which divides the simulation domain into a set of nodes and grid points. By solving these equations across the grid, the carrier transport mechanisms within the structure are accurately modeled. This finite-element approach enables a comprehensive simulation of the solar cell's performance [64].

The simulation of the TiO_2/$BiFeO_3$/Spiro-OMeTAD solar cell was performed in COMSOL using a systematic approach. First, the 1D geometry of the device, including the TiO_2 electron transport layer, $BiFeO_3$ absorber, and Spiro-OMeTAD hole transport layer, was defined with precise thicknesses. Material properties, such as bandgap, electron affinity, carrier mobility, and permittivity, were assigned based on reported values. Ideal ohmic contacts were applied at the electrodes, and a fine mesh was generated throughout the solar cell structure, with increased density at the interfaces between TiO_2/$BiFeO_3$ and $BiFeO_3$/Spiro-OMeTAD layers to accurately capture variations in carrier concentration and electric field. The semiconductor physics module solved the coupled Poisson, continuity, and drift-diffusion equations to model charge transport and carrier generation. Illumination with the AM1.5 solar spectrum provided the photo-generation rate in the absorber layer and cross-sectional area was used as 4×10^{-12} m^2. Steady-state simulations were performed for varying thicknesses, transport layer properties, and operating temperatures. Finally, current density-voltage (J-V) characteristics were extracted, ensuring a thorough evaluation of device performance.

3. Device simulation and methodology

3.1 Solar absorption and solar spectrum

The solar spectrum represents the distribution of solar energy across different wavelengths. Fig. 1(a) shows that solar irradiance increases sharply to a peak of about 1.6 $Wm^{-2}nm^{-1}$ at 460 nm. Beyond this point, it gradually declines up to 2500 nm due to the combined effects of decreasing solar blackbody emission intensity at longer wavelengths and absorption by atmospheric gases such as water vapor, oxygen, and carbon dioxide. This demonstrates the wavelength-dependent nature of solar irradiance, where shorter wavelengths exhibit stable intensity and longer

View Article Online
DOI: 10.1039/D5MA01257K

wavelengths show a progressive decrease [65]. The refractive index (n) and extinction coefficient (k) are critical parameters that define a material's optical properties, both of which exhibit wavelength-dependent variations. The n initially increases with wavelength due to the dispersion phenomenon, where light bending intensifies as it interacts with the material and for wavelengths beyond 0.4 µm, n begins to decrease, stabilizing at longer wavelengths (above 1 µm) as shown in Fig. 1(b). In contrast, k initially decreases with increasing wavelength, particularly beyond 0.3 µm. This behavior arises from electronic transitions within the material, reflecting its distinct interaction with incident light and beyond 0.5 µm, k stabilizes, indicating minimal further absorption. The interplay of n and k demonstrates their influence on light transmission, reflection, and absorption in the material [66]. The generation of electron-hole (e/h) pairs is governed by the interaction of incident light with the material and when photons are absorbed, electrons transition from the valence band to the conduction band, creating e/h pairs [67]. In Fig. 1(c), arc length indicates the total thickness of optimized layers in this solar cell device. The e/h pair generation is maximum within the 100 to 500 nm arc length approximately, signifying the high absorption and carrier generation and beyond 500 nm, the generation rate declines and stabilizes, implying less pair generation for longer arc length. This behavior underscores the critical role of arc length in maximizing the photo-generated carrier densities [68].

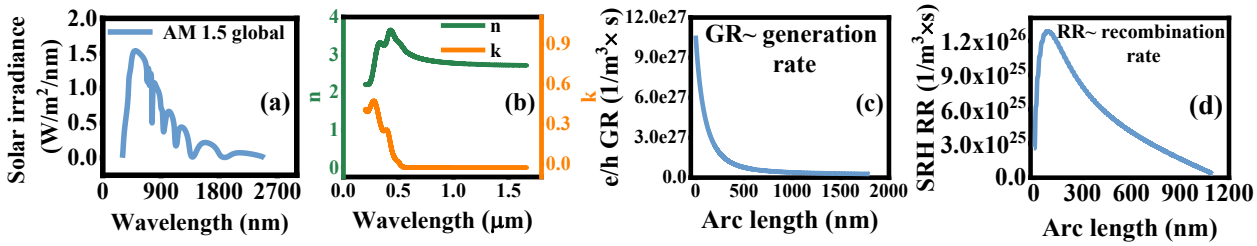

Figure 1(a) Solar spectrum, **(b)** n,k dependence on wavelength, **(c)** generation rate of e/h pairs inside the layers of solar cell, and **(d)** Shockley-Read-Hall recombination rate within the device (2-column fitting image)

After generation, the Shockley-Read-Hall (SRH) recombination occurs, a process involving electron-hole recombination facilitated by material defects or impurities, also exhibits wavelength-dependent characteristics. At smaller arc length, SRH recombination peaks, reaching a maximum value of approximately 1.3×10^{26} ($1/m^3\times s$) at around 100 nm as shown in Fig. 1(d). With increasing arc length, the SRH recombination rate declines sharply, highlighting its sensitivity to changes in arc length. This reduction is attributed to variations in carrier

View Article Online
DOI: 10.1039/D5MA01257K

concentrations and the density of trapping centers that modulate the recombination dynamics. The observed trends emphasize the critical interplay between recombination mechanisms and material properties under varying spectral conditions [69].

3.2 Energy band structure

Fig. 2(a, b) presents the architecture of a multi-layer PV cell comprising TiO_2/BFO/Spiro-OMeTAD as its primary constituents and each layer in this design is chosen for its unique properties to optimize solar light absorption, charge separation, and efficient carrier transport, ultimately enhancing the device's power generation efficiency [70]. The operation of this device is supported by material-specific characteristics and semiconductor physics, both of which have been extensively studied and validated in this study. The TiO_2 layer, positioned at the top, serves as the ETL due to its wide E_g and high electron mobility. These properties render TiO_2 highly transparent to sunlight, allowing most incident photons to penetrate the underlying BFO layer for absorption.

Materials with increased thickness exhibit enhanced absorption of low-energy photons due to their larger penetration depth. Conversely, high-energy photons, such as those in the near-ultraviolet spectrum, have higher absorption coefficients, resulting in reduced penetration depths. Fig. 2(c) shows that the conduction band level (E_c) and the Fermi level for electrons (E_{fn}) indicates that energy remains constant as material thickness increases, up to approximately 75 nm. Beyond this threshold, the energy begins to rise, reaching a value of 2.88 eV and for thinner materials, the absorption of higher-energy photons predominates due to their shorter penetration depths. In contrast, low-energy photons in the near-infrared region exhibit lower absorption coefficients, allowing deeper penetration into the material. The relationship between the Fermi level for holes (E_{fp}) and the valence band level (E_v) demonstrates that the carrier energy initially starts at low negative values and gradually increases, reaching zero as energy levels align. The E_g energies of the studied materials vary significantly: spiro materials exhibit the highest E_g energy, followed by BFO with an intermediate E_g, and TiO_2 with the lowest E_g energy. These variations highlight the distinct electronic properties of these materials at varying thicknesses [71]. The observed trends suggest a direct correlation between material thickness and E_g energy: as the thickness increases, the E_g energy also rises. This behavior underscores the influence of material geometry on its optical and electronic properties, emphasizing the importance of thickness-dependent optimization for tailored PV or optoelectronic performance.

View Article Online
DOI: 10.1039/D5MA01257K

Moreover, TiO_2 effectively facilitates electron transport to the top contact while minimizing electron-hole recombination, a critical factor for maintaining charge separation. The BFO layer, a multiferroic PVK with a E_g of 2.2 eV, acts as the main light-absorbing component of the device. BFO absorbs photons across a significant portion of the visible spectrum, leading to the generation of excitons upon photoexcitation [34]. The FE properties of BFO aid in separating these excitons, directing electrons toward the TiO_2 and holes toward the bottom HTL, Spiro-OMeTAD and this transportation is shown in Fig. 2(d). Spiro-OMeTAD, positioned at the bottom of the cell, works as the HTL, facilitating hole transport from the BFO layer to the bottom contact [72]. By ensuring efficient hole transport and suppressing recombination with electrons, this layer supports sustained charge separation and a steady flow of electric current. The functionality of this PV cell is governed by the principles of semiconductor band theory, particularly the energy band alignment among the layers. The alignment between BFO and Spiro-OMeTAD supports downward hole transport, while the wide E_g of TiO_2 prevents electron recombination, directing electrons toward the top contact.

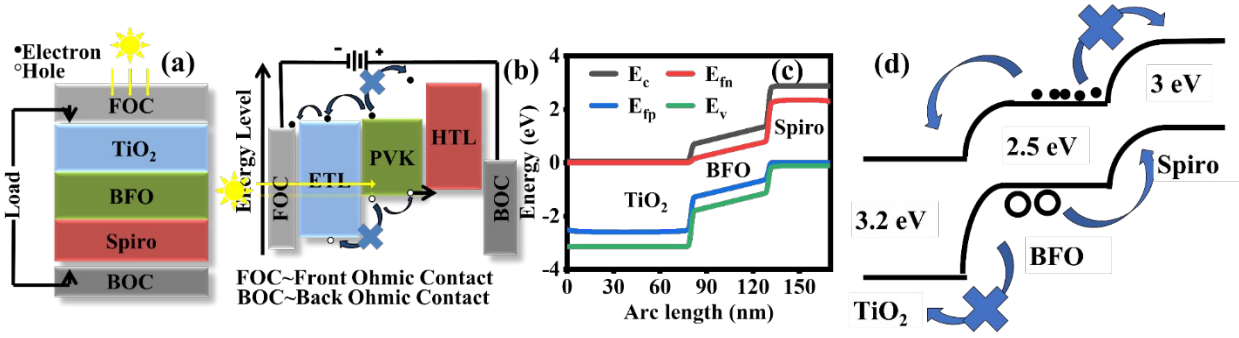

Figure 2(a) Solar cell's schematic, **(b)** schematic with energy levels, **(c)** energy level variations vs arc length, and **(d)** energy band alignment of TiO_2/BFO/Spiro-OMeTAD heterojunction solar cell for transportation of charge carriers (2-column fitting image)

Although a dedicated interfacial recombination analysis was not presented as a separate section, its impact is inherently embedded within the simulated current-voltage characteristics and directly contributes to the observed current saturation behavior. The interfacial regions between adjacent layers were modeled under charge-neutral conditions, with a surface charge density of 0 C/cm^2, thereby eliminating artificial fixed charges and maintaining electrostatic equilibrium across the junctions. To accurately describe recombination dynamics at these interfaces, the SRH trapping mechanism was employed, assigning both electron and hole surface recombination velocities of

View Article Online
DOI: 10.1039/D5MA01257K

1000 cm/s. These parameters fall within experimentally reported ranges for perovskite and oxide-based heterojunctions, ensuring physically consistent interfacial kinetics. The trap energy level was positioned at the midgap, corresponding to a neutral defect state with zero offset from the intrinsic Fermi level, thereby representing symmetric recombination for electrons and holes. Furthermore, the interface continuation feature in COMSOL Multiphysics was enabled to preserve numerical convergence and physical continuity across the heterointerfaces, ensuring reliable simulation of interfacial charge transport and recombination phenomena.

The properties of TiO_2, BFO, and Spiro-OMeTAD enable effective photon absorption, charge carrier separation, and transport within the multi-layer PV cell. Careful band alignment and material selection, as supported by extensive research in PV technology, contribute to a highly efficient system capable of converting solar energy into electricity with reduced recombination losses. The optimized input parameters for TiO_2, BFO, and Spiro-OMeTAD materials assuming the ideal ohmic front and back contacts, are tabulated in Table 1.

Table 1 Initial parameters of materials used for respective layers in 1D TiO_2/BFO/spiro OMeTAD PSC

Material properties	TiO_2	BFO	spiro-OMeTAD
Thickness (nm)	80	50	40
Energy band gap (eV)	3.2	2.5	3
Electron affinity (eV)	3.9	3.3	1.9
Relative permittivity	9	6	3
C.B effective density of states 'N_C' (cm^{-3})	1×10^{20}	5×10^{18}	1×10^{20}
V.B effective density of states 'N_V' (cm^{-3})	2×10^{20}	5×10^{18}	1×10^{20}
Electron mobility 'μ_n' (cm^2/V. s)	20	80	2
Hole mobility 'μ_h' (cm^2/V. s)	25	25	1×10^{-2}
Electron lifetime, SRH, (ns)	1	1	5
Hole lifetime, SRH, (ns)	1	1	5
Reference	[73]	[74]	[75]

4. Results and discussion

4.1 Effect of BFO's thickness on PV performance

The absorbing layer such as BFO, acts as active region of solar cell, helps to generate the photo-induced charge carriers which further migrate towards their respective electrodes. For this,

View Article Online
DOI: 10.1039/D5MA01257K

the thickness of absorbing layer is very crucial because as its thickness increases it may increase the absorption of light and ultimately enhances the photo-induced charge carriers. But, on the other hand, after this optimum thickness, it may reduce the performance of solar cell by increasing the internal resistance and defects. Fig. 3(a) presents the schematic illustration to visualize the effect of thickness of absorbing layer, and it is obvious that by increasing thickness of this layer beyond its optimal value, it may increase the number of defects as depicted by small circle. Fig. 3(b) shows the J-V characteristics of the solar cell for different BFO thicknesses, where J_{sc} increases with increasing BFO thickness. At 50 nm, J_{sc} is around 3.69 mA/cm^2, while at 1850 nm, it reaches approximately 9.004 mA/cm^2, indicating improved charge collection for thicker layers. The sharp decline occurs at different voltages, with thinner layers dropping around 1.6–2.0 V and thicker layers around 1.3 V, suggesting that increased thickness lowers V_{oc} due to higher recombination losses. Fig. 3(c) shows P-V curves for different BFO thicknesses, where maximum power density increases with thickness. Thinner layers peak around 1.6–2.0 V, while thicker layers peak near 1.3–1.5 V, shows higher thickness enhances power generation, but excessive thickness may cause recombination losses, affecting efficiency.

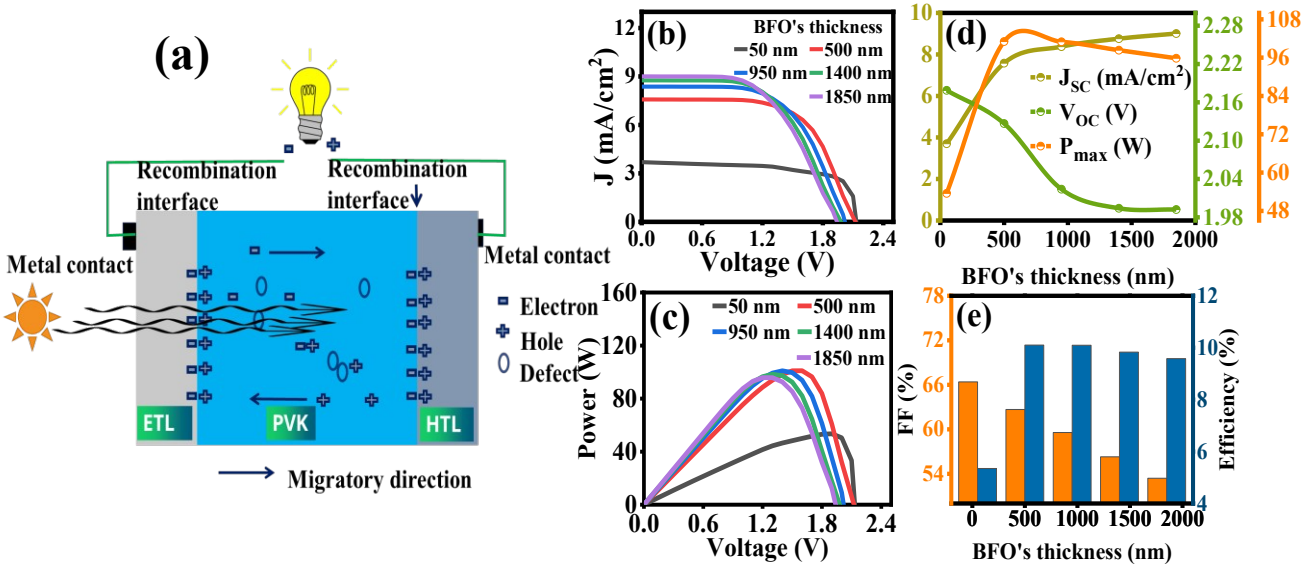

Figure 3(a) Schematic illustration of effect of absorbing layer's thickness on performance of solar cell, **(b)** J-V curve, **(c)** P-V curve of TiO_2/BFO/Spiro-OMeTAD solar cell and effect of BFO's thickness variation on, **(d)** J_{sc}, V_{oc}, P_{max}, and **(e)** %FF & %efficiency (2-column fitting image)

Fig. 3(d) presents the variation in J_{sc}, V_{oc}, and P_{max} at different thicknesses of BFO, and it shows that by varying the thickness from 50 to 1850 nm, the J_{sc} exhibits a steady increase with

View Article Online
DOI: 10.1039/D5MA01257K

thickness, rising from 3.697 mA/cm^2 at 50 nm to a maximum of 9.004 mA/cm^2 at 1850 nm. This behavior is a result of enhanced photon absorption as thickness increases, which facilitates the generation of a greater number of charge carriers, and the contribution of longer-wavelength photons becomes significant at larger thicknesses, further boosting J_{sc}. Furthermore, V_{oc} decreases from 2.178 V at 50 nm to 1.994 V at 1400 nm, then remains constant up to 1850 nm. This indicates that increasing BFO thickness initially increases recombination losses, but beyond 1400 nm, its impact stabilizes. On the other hand, the P_{max} of 53.485 W at 50 nm, increase to 104.5 W at 631 nm and then declines to 95.79 W reaching at 1850 nm. The rise in P_{max} up to 631 nm results from optimal photon absorption and minimal recombination losses and beyond this thickness, higher recombination rates and defect densities limit the charge carrier generation, reducing P_{max}. Moreover, Fig. 3(e) shows fill factor (FF) and efficiency (η) dependence on BFO thickness, and FF gradually decreases from 66.39% (at 50 nm) to 53.40% (at 1850 nm). Conversely, as the BFO thickness increases, the η of solar cell reaches a maximum at an optimal thickness and decreases beyond this point. At 50 nm, the η is 5.34%, increasing to a peak value of 10.101% at 500 nm. Beyond this optimal thickness, the η decreases to 9.579% at 1850 nm. The increase in η up to the optimal thickness is attributed to enhanced photon absorption, particularly for photons with longer wavelengths, leading to improved charge carrier generation. However, beyond 500 nm, the η decreases due to increased recombination rates, which reduce charge carrier lifetimes and limit charge carrier generation [76]. All the output characteristics with variation in BFO's thickness are enlisted in Table 2.

Table 2 Designed device 1D (TiO_2/BFO/spiro-OMeTAD) performance parameters with varying absorber layer's (BFO) thickness

BFO's thickness (nm)	J_{sc} (mA/cm^2)	V_{oc} (V)	P_{max} (W)	FF (%)	Efficiency (%)
50	3.697	2.179	53.485	66.392	5.349
500	7.578	2.127	101.018	62.676	10.102
950	8.373	2.024	100.957	59.571	10.095
1400	8.758	1.994	98.319	56.295	9.831
1850	9.004	1.992	95.794	53.405	9.5793

4.2 Effect of ETL's thickness variation on PV performance

View Article Online
DOI: 10.1039/D5MA01257K

Thinner ETL is best for the maximum output yield of solar cell, as its thickness increases, it may cause hinderance to the incident light that must reach at absorbing layer, and secondly it enhances the series resistance of solar cell. Fig. 4(a) presents the schematic illustration of working of solar cell, having thinner ETL, and it is clear that incident light can reach at active region of solar cell easily. But, if the ETL is thicker, it stops the incident light, as depicted in Fig. 4(b). Fig. 4(c) illustrates J-V response at different ETL thicknesses, ranging from 10 to 150 nm, J_{sc} decreases with increasing ETL thickness. The sharp J_{sc} drop occurs at 1.6 V for all thicknesses, indicating higher resistance and recombination losses in thicker ETL layers. P-V response is used to determine the P_{max} of solar cell, as shown in Fig. 4(d), power peaks around 100.95 W at 10 nm ETL and decreases to 56.76 W at 150 nm. Thinner layers achieve higher power, while thicker layers reduce output due to increased resistance, P decline sharply within 1.6–2.0 V. It is observed that thinner ETL improve electron transport and light absorption, maximizing current density while thicker layers on the other hand hinder these processes by increasing resistance and reducing light penetration.

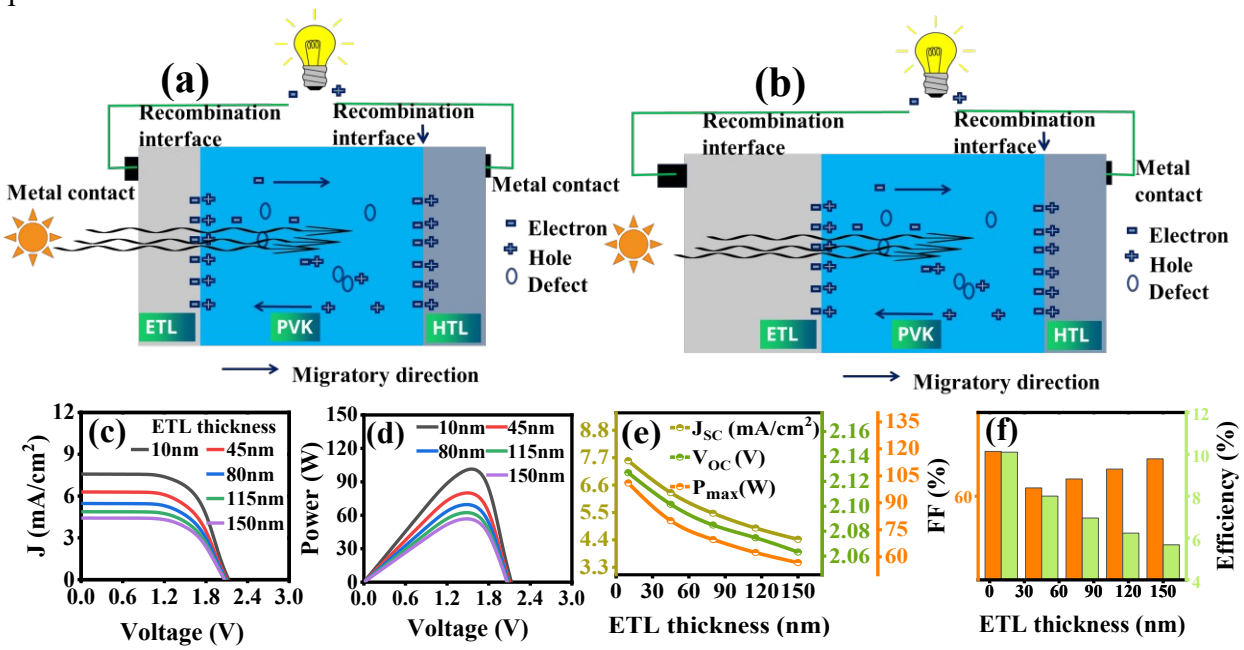

Figure 4(a) Schematic illustration of effect of ETL's thickness on performance of solar cell; thinner ETL, **(b)** thicker ETL, **(c)** J-V curve, **(d)** P-V curve of TiO_2/BFO/Spiro-OMeTAD solar cell and effect of ETL's thickness variation on, **(e)** J_{sc}, V_{oc}, P_{max}, and **(f)** %FF, and %efficiency (2-column fitting image)

View Article Online
DOI: 10.1039/D5MA01257K

Fig. 4(e) shows the variation in J_{sc}, V_{oc}, and P_{max} at different thicknesses of ETL, and the J_{sc} decreases from 7.57 to 4.420 mA/cm^2, and similarly, the V_{oc} decreases (from 2.126 to 2.063 V) as thickness increases (from 10 to 150 nm), suggesting that V_{oc} is sensitive to ETL thickness, with optimal performance occurring at thinner layer. Thinner ETL layers help maintain better voltage due to efficiency charge transport, while thicker layers introduce more resistance, resulting in a reduced value. Moreover, the P_{max} decreases (101.01 to 56.76 W) with increasing ETL thickness due to higher recombination and resistive losses. Fig. 4(f) depicts the variation in % FF and η, FF decreases from 62.67% at 10 nm to its lowest at 45 nm, then gradually increases to 62.23% at 150 nm. This suggests that moderate ETL thickness increases resistance and recombination, but thicker layers stabilize FF. On the other hand, a consistent decline can be seen in overall η as ETL thickness increases, as the thinner ETLs ensure efficient charge transport, minimal recombination, and better light penetration, while thicker layers impede performance due to higher resistance, increased recombination, and reduced photon absorption by the active layer [77]. The detailed numerical values for these output characteristics with variation in ETL's thickness, are listed in Table 3.

Table 3 Designed device 1D (TiO_2/BFO/spiro-OMeTAD) performance parameters with varying ETL's (TiO_2) thickness

TiO_2's thickness (nm)	J_{sc} (mA/cm^2)	V_{oc} (V)	P_{max} (W)	FF (%)	Efficiency (%)
10	7.578	2.126	101.017	62.673	10.101
45	6.295	2.101	80.035	60.492	8.003
85	5.466	2.084	69.559	61.028	6.955
115	4.876	2.074	62.335	61.619	6.233
150	4.420	2.063	56.76	62.230	5.676

4.3 Effect of HTL's thickness variation on PV performance

The role of shunt resistance in the performance of solar cell is remarkable, specially it affects the V_{oc}, and it can be understood in this sense, as HTL thickness increases it provides unwanted paths to the internal current and due to which shunt resistance decreases and it ultimately reduces the V_{oc}, as shown in Fig. 5(a, b). Furthermore, the J-V and P-V characteristics at different thicknesses of HTL, ranging from 50 to 150 nm, to determine the J_{sc}, V_{oc}, and P_{max}, as shown in Fig. 5(c) and Fig. 5(d), respectively. J_{sc} remains nearly constant before sharply dropping, while P

View Article Online
DOI: 10.1039/D5MA01257K

increases, before a sharp decline at 1.6 V; both parameters show minimal variation across different HTL thicknesses. Fig. 5(e) presents the variation in J_{sc}, V_{oc}, and P_{max}, and the J_{sc} increases from 7.57 mA/cm^2 at 10 nm to 7.74 mA/cm^2 at 150 nm due to improved charge collection and reduced carrier recombination with increasing HTL thickness, enhancing current extraction efficiency. On the other hand, the V_{oc} exhibits a gradual decrease (from 2.1268 to 2.1058 V) with increasing HTL (from 10 to 150 nm), likely resulting from energy level mismatch and shunt resistance in thicker layers. Moreover, the P_{max} increases as the thickness increases, peaking to 103.45 W at an HTL thickness of 150 nm and may saturate after this optimal value of thickness. Furthermore, FF improves with increasing HTL thickness up to the optimum range and finally, the η increases steadily from 10.10% to 10.34%, as shown in Fig. 5(f). These findings underscore the critical role of optimizing HTL thickness to achieve a balance between efficient charge transport and resistive losses, and properly tuned HTL thickness enhances the overall device performance, achieving maximum η and power output for PSCs [78]. Table 4 presents the comprehensive overview of all these output characteristics with variation in HTL's thickness.

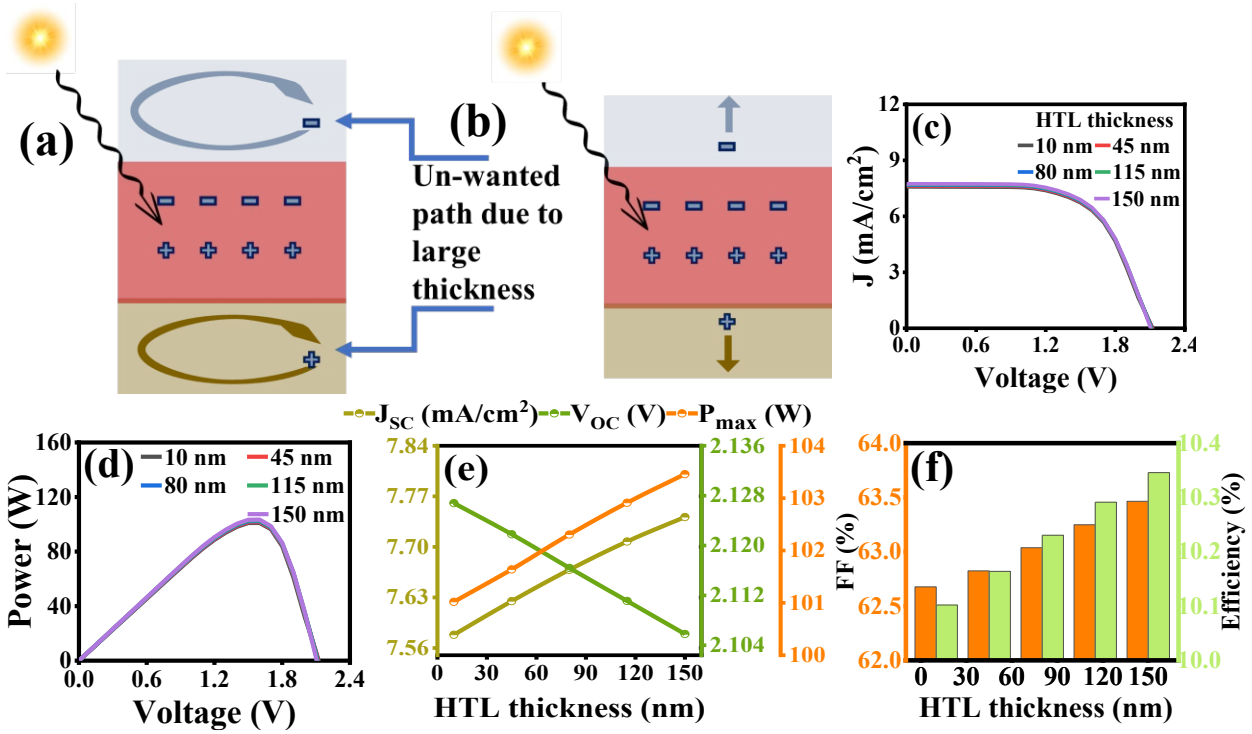

Figure 5(a,b) Schematic illustration of effect of thicker and thinner HTL on performance of solar cell, **(c)** J-V curve, **(d)** P-V curve of TiO_2/BFO/Spiro-OMeTAD solar cell and effect of HTL's thickness variation on, **(e)** J_{sc}, V_{oc}, P_{max}, and **(f)** %FF & %efficiency (2-column fitting image)

View Article Online
DOI: 10.1039/D5MA01257K

4.4 Effect of BFO's DOS of conduction and valence band (N_CN_V) on PV performance

It is important to study the density of states (DOS) in conduction as well as valence band, because it is directly linked with the carrier's transportation and recombination process. Fig. 6(a) shows the higher DOS at conduction band, reflecting the greater probability of intra-band transition, which is non-radiative emission of energy and this happens beyond an optimal level, but its probability is lesser under the optimum range of DOS. Similarly, the higher DOS at valence band makes the greater probability of intra-band transition as well, as shown in Fig. 6(b). Fig. 6(c) shows that as N_CN_V increases from 2×10^{17} to 2×10^{20} cm^{-3}, J_{sc} remains nearly constant, but the V_{oc} at which it sharply drops shifts to lower values, indicating an increase in recombination and a reduction in charge extraction efficiency. Fig 6(d) illustrates the P-V characteristics, the P initially rises, peaks, and then declines at higher voltages. The shifting peak suggests that higher N_CN_V values influence recombination dynamics, impacting the optimal operating voltage and reducing overall power extraction.

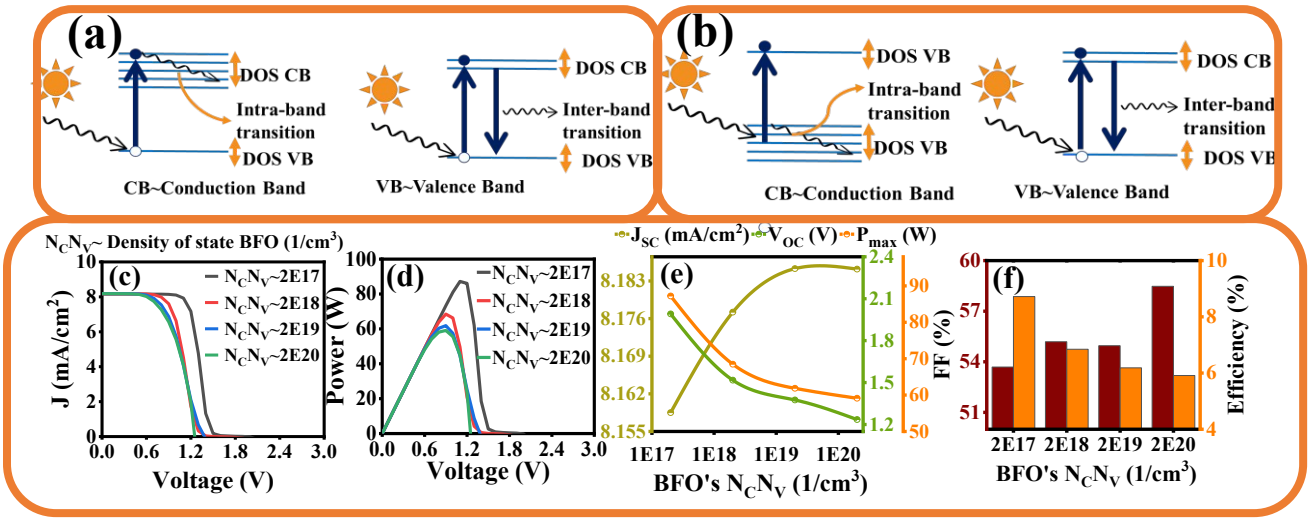

Figure 6(a,b) Schematic illustration of higher & lower density of states (DOS) for conduction & valence band (N_CN_V) within $BiFeO_3$ (BFO) layer, **(c)** J-V curve, **(d)** P-V curve of TiO_2/BFO/Spiro-OMeTAD solar cell and effect of BFO's N_CN_V on **(e)** J_{sc}, V_{oc}, P_{max}, **(f)** %FF and %efficiency (2-column fitting image)

In Fig. 6(e), although J_{sc} slightly increases from 8.158 mA/cm^2 to 8.185 mA/cm^2, V_{oc} significantly decreases from 1.99 V to 1.235 V, resulting in a reduction of P_{max} from 87.21 W to 59.117 W. The decrease in V_{oc} with an increase in the effective density of states strongly confirms their inverse relationship, highlighting a fundamental trade-off in device performance. This occurs

View Article Online
DOI: 10.1039/D5MA01257K

because the higher density of states enhances recombination losses, which reduces the built-in potential and the V_{oc}, while the slight improvement in J_{sc} due to increased carrier generation cannot compensate for the major voltage drop, leading to lower maximum power [79]. In Fig. 6(f), the FF increases from 53.68% to 58.47%, indicating improved charge extraction and reduced resistive losses at higher N_CN_V. However, η decreases from 8.72% to 5.91%, mainly due to the significant drop in V_{oc} and P_{max}, which outweighs the benefits of the FF improvement. This suggests that excessive increase in N_CN_V leads to higher recombination, negatively impacting overall performance. The Table 5 presents the influence of N_CN_V variations on overall device performance, showing trends in electrical characteristics and η as the density of states increase.

Table 4 Designed device 1D (TiO_2/BFO/spiro-OMeTAD) performance parameters with varying HTL's (spiro) thickness

Spiro's thickness (nm)	J_{sc} (mA/cm^2)	V_{oc} (V)	P_{max} (W)	FF (%)	Efficiency (%)
50	7.578	2.126	101.019	62.676	10.102
150	7.624	2.121	101.638	62.823	10.163
80	7.668	2.116	102.304	63.037	10.230
115	7.707	2.111	102.912	63.248	10.291
150	7.741	2.105	103.457	63.464	10.345

Table 5 Designed device 1D (TiO_2/BFO/spiro-OMeTAD) performance parameters with varying BFO's density of states in conduction & valence bands (N_CN_V)

BFO's N_CN_V (cm^{-3})	J_{sc} (mA/cm^2)	V_{oc} (V)	P_{max} (W)	FF (%)	Efficiency (%)
2×10^{17}	8.158	1.991	87.216	53.721	8.721
2×10^{18}	8.177	1.517	68.468	55.187	6.846
2×10^{19}	8.185	1.375	61.854	54.954	6.185
2×10^{20}	8.185	1.235	59.117	58.476	5.911

4.5 Effect of ETL's DOS of conduction and valence band (N_CN_V) on PV performance

Fig. 7(a) illustrates the J-V characteristics for different TiO_2 density of states (N_CN_V). As N_CN_V increases from 2×10^{15} to 2×10^{18} cm^{-3}, the J_{sc} remains stable at lower voltages but drops sharply at higher voltages. Higher N_CN_V shifts the cutoff point, affecting the V_{oc} and indicating changes in charge transport and recombination. Fig. 7(b) presents P-V characteristics for varying

View Article Online
DOI: 10.1039/D5MA01257K

TiO_2'N_CN_V, P increases, peaks, and then declines. Higher DOS shifts the peak position and alters maximum power, highlighting its effect on solar cell performance.

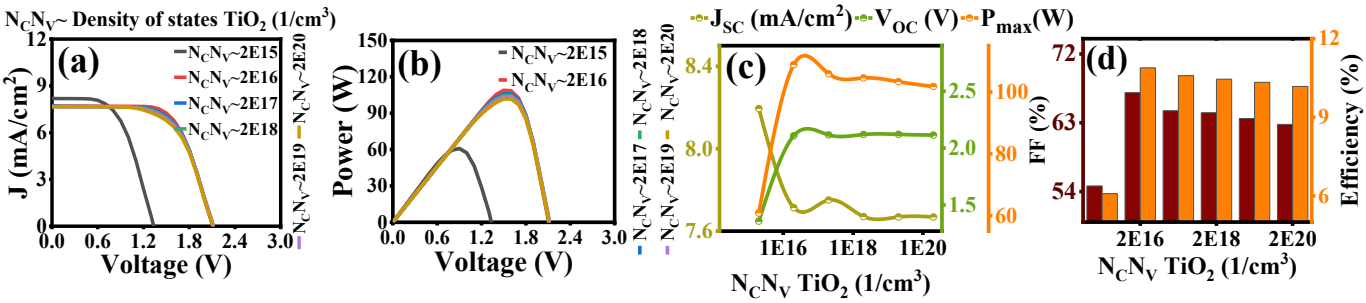

Figure 7 Effect of density of states within conduction and valence band (N_CN_V) in electron transport layer (TiO_2) in solar cell performance, **(a)** J-V curve, **(b)** P-V curve of TiO_2/BFO/Spiro-OMeTAD solar cell and effect of TiO_2's N_CN_V on **(c)** J_{sc}, V_{oc}, P_{max}, **(d)** %FF and %efficiency (2-column fitting image).

Table 6 Designed device 1D (TiO_2/BFO/spiro-OMeTAD) performance parameters with varying TiO_2' density of states in conduction and valence bands (N_CN_V)

TiO_2's N_CN_V (cm^{-3})	J_{sc} (mA/cm^2)	V_{oc} (V)	P_{max} (W)	FF (%)	Efficiency (%)
2×10^{15}	8.194	1.357	60.871	54.727	6.087
2×10^{16}	7.713	2.108	108.877	66.940	10.887
2×10^{17}	7.750	2.115	105.899	64.575	10.589
2×10^{18}	7.670	2.119	104.556	64.315	10.455
2×10^{19}	7.668	2.120	103.353	63.552	10.335
2×10^{20}	7.668	2.114	101.784	62.781	10.178

Fig. 7(c) shows variation in J_{sc}, V_{oc}, and P_{max}, as N_CN_V increases from 2×10^{15} cm^{-3} to 2×10^{20} cm^{-3}, J_{sc} decreases from 8.194 mA/cm^2 to 7.6 mA/cm^2 and then stabilizes due to saturation in charge carrier transport. V_{oc} increases from ~1.35 V to ~2.1 V, indicating improved band alignment with minimal effect at higher, while P_{max} increases from ~60.87 W to ~108.87 W, then levels off, as recombination counteracts further gains. Moderate enhances performance, but excessive values lead to saturation. Fig. 7(d) shows the variation of FF and η with the N_CN_V in TiO_2, FF increases from 54% to 66%, stabilizing or a very little decline afterward due to improved charge transport. Moreover, the η follows a similar trend, rising from 6.08% to 10.88%, then plateauing as further increases no longer significantly enhance performance [80]. The

View Article Online
DOI: 10.1039/D5MA01257K

improvement is due to reduced recombination and better carrier collection, but excessive leads to diminishing returns. Table 6 highlights the impact of ETL's N_CN_V variations on solar cell performance, showcasing key trends and dependencies.

4.6 Effect of BFO's electron affinity (χ) on PV performance

The energy band alignment is crucial for the efficient operation of solar cells; any discontinuity or misalignment can lead to erroneous results. Therefore, ensuring proper energy band alignment across the three layers requires careful optimization of electron affinity. χ is referred to the energy difference between the vacuum energy level and the conduction band minimum of a material. It governs the energy band alignment at heterojunction interfaces and significantly affects charge transfer and recombination dynamics within the solar cell. Therefore, its optimization is essential for achieving efficient carrier transport and high device performance. For the influence of varying χ of the absorber layer (BFO) on the operation performance of solar cell, J-V characteristics shows in Fig. 8(a) that J_{sc} remains nearly constant, while the V_{oc} drop shifts with χ. At 3.3 eV, the drop starts around 0.9 V, at 3.4 eV around 1.0 V, and at 3.5 eV beyond 1.2 V, shows higher χ improves charge transport, reducing voltage losses. In Fig. 8(b) P-V characteristics displays that P increases with voltage, peaks, and then declines, the highest peak occurs at 3.3 eV, while 3.4 eV and 3.5 eV show lower peaks, indicating that lower χ favors maximum power output.

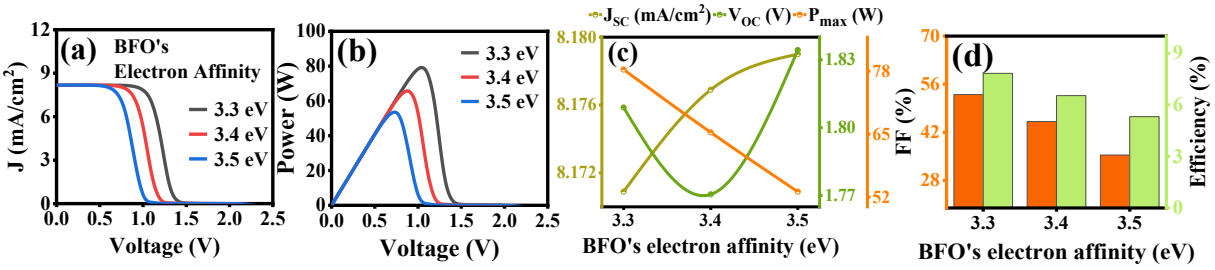

Figure 8(a) J-V curve, **(b)** P-V curve of TiO_2/BFO/Spiro-OMeTAD solar cell and effect of $BiFeO_3$ (BFO)'s electron affinity on **(c)** J_{sc}, V_{oc}, P_{max}, and **(d)** %FF and %efficiency (2-column fitting image).

Furthermore, Fig. 8(c) presents the variation in J_{sc}, V_{oc}, and P_{max} at different χ values, and it is clear that J_{sc} increases slightly from 8.171 mA/cm^2 at 3.3 eV to 8.179 mA/cm^2 at 3.5 eV, indicating improved charge extraction with higher χ. V_{oc} first decreases from 1.81V at 3.3 eV to 1.77 V at 3.4 eV, then increases to 1.83 V at 3.5 eV, suggesting an initial rise in recombination at

View Article Online
DOI: 10.1039/D5MA01257K

3.4 eV before better band alignment at 3.5 eV improves voltage. P_{max} continuously decreases from 78 W to 55 W, implying that increasing χ introduces losses that outweigh the gains in charge transport, reducing overall device performance. However, FF decreases significantly from 55.40% to 38.98%, indicating that higher χ negatively impacts charge extraction and increases resistive losses. Similarly, η declines from 8.50% to 5.80%, which follows the trend of decreasing P_{max} shown in Fig. 8(d). This η reduction is directly linked to energy band misalignment, leading to compromised charge extraction and increased recombination [76]. In the end, all the output characteristics with variation in BFO's electron affinity, are enlisted in Table 7.

Table 7 Designed device 1D (TiO_2/BFO/spiro-OMeTAD) performance parameters with varying BFO's electron affinity

BFO's affinity (eV)	J_{sc} (mA/cm^2)	V_{oc} (V)	P_{max} (W)	FF (%)	Efficiency (%)
3.3	8.170	1.808	78.317	52.987	7.831
3.4	8.176	1.770	65.361	45.147	6.536
3.5	8.179	1.834	53.127	35.411	5.312

4.7 Effect of TiO_2's electron affinity (χ) on PV performance

The performance of a solar cell is significantly influenced by the χ of the TiO_2 layer and variations in this parameter impact key electrical characteristics. Fig. 9(a) shows J-V characteristics for different TiO_2' χ values (3.5 eV to 3.7 eV). The sharp drop in J occurs around 1.6 V, indicating the turn-off point. The overall J_{sc} remains relatively stable before this V_{oc}, suggesting minimal impact of χ on current generation until a critical voltage is reached. Fig. 9(b) illustrates the P-V curve for different TiO_2 electron affinities, P rises, peaks, and then drops sharply. The peak power remains nearly constant, indicating minimal impact of electron affinity on power output. However, slight differences may be attributed to changes in charge transport and recombination dynamics within the device.

Fig. 9(c) depicts the variations in J_{sc}, V_{oc}, and P_{max} with changing TiO_2's χ, J_{sc} fluctuates within a narrow range of 8.1685 to 8.1700 mA/cm^2, showing a peak around 3.6 eV, while dipping at intermediate values, which indicates that specific electron affinities enhance charge extraction, improving current generation. V_{oc} follows a same pattern like J_{sc}, ranging between 1.49 V and 1.53 V, reaching its maximum at 3.6 eV. This behavior suggests that band alignment at these electron affinities optimally supports voltage generation. P_{max} remains relatively stable, fluctuating slightly

View Article Online
DOI: 10.1039/D5MA01257K

between 48.801 W and 48.785 W, as the compensatory effects of J_{sc} and V_{oc} balance the overall power output. The observed trends indicate that optimizing electron affinity is crucial for enhancing solar cell performance without significantly affecting power stability. Fig. 9(d) indicates the variation of FF and η with TiO_2 electron affinity, FF ranges between 39.90% and 38.90%, reaching its highest values around 3.5 eV, and similarly, η peaks at 4.884% for 3.5 eV. When the χ is optimal, the conduction band alignment enhances electron flow, reducing recombination losses and thereby increasing η. These findings emphasize the critical role of optimizing TiO_2's χ to balance energy alignment, minimize recombination, and enhance charge transport for achieving superior solar cell performance [81]. Finally, the output values with variation in electron affinity of TiO_2, are listed in Table 8.

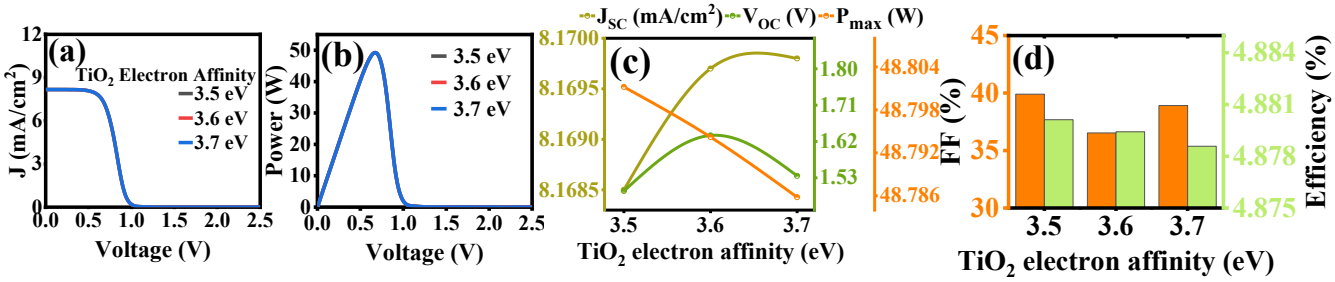

Figure 9(a) J-V curve, **(b)** P-V curve of TiO_2/BFO/Spiro-OMeTAD solar cell and effect of electron affinity of TiO_2 on **(c)** J_{sc}, V_{oc}, P_{max}, and **(d)** %FF and %efficiency (2-column fitting image).

Table 8 Designed device 1D (TiO_2/BFO/spiro-OMeTAD) performance parameters with varying TiO_2's electron affinity

TiO_2's affinity (eV)	J_{sc} (mA/cm^2)	V_{oc} (V)	P_{max} (W)	FF (%)	Efficiency (%)
3.5	8.168	1.497	48.801	39.903	4.880
3.6	8.169	1.634	48.794	36.531	4.879
3.7	8.169	1.534	48.785	38.909	4.878

4.8 Effect of Spiro's electron affinity (χ) on PV performance

Fig. 10(a) illustrates the J-V curve, where J_{sc} remains constant (8.167 mA/cm^2) up to 0.6-1.1 V before decreasing to near-zero at higher voltages, this is attributed to better energy level alignment, enhancing photon-to-electron conversion. Fig. 10(b) demonstrates the P-V curve, with P increasing to a peak (78.32 W) as χ rises from 1.5 to 1.9 eV. Fig. 10(c) presents the variation in J_{sc}, V_{oc}, and P_{max} for different χ values of Spiro, and it is observed that J_{sc} increases from 8.167 to

View Article Online
DOI: 10.1039/D5MA01257K

8.169 mA/cm^2 with rising χ, due to improved symmetry in energy levels and enhanced charge carrier flow across the device. On the other hand, V_{oc} initially increases then slightly decreases as χ increases, attributable to minimized bandgap mismatches between the absorber and HTL layers, which slightly diminish charge separation efficiency. However, the P_{max} improves linearly from 48.78 to 78.32 W. These enhancements result from improved energy level alignment between HTL and the PVK layer, which minimizes energy losses and charge transport efficiency. Similarly, FF and η increases as shown in Fig. 10(d), and FF increases from 34.11 to 53.13% while η increases from 4.878% at χ=1.5 eV to 7.832% at χ =1.9 eV. These results highlight the critical role of HTL electron affinity in optimizing PSCs performance [82]. In the end, Table 9 presents the comprehensive overview of all the above-mentioned output characteristics with variation in electron affinity of Spiro-OMeTAD.

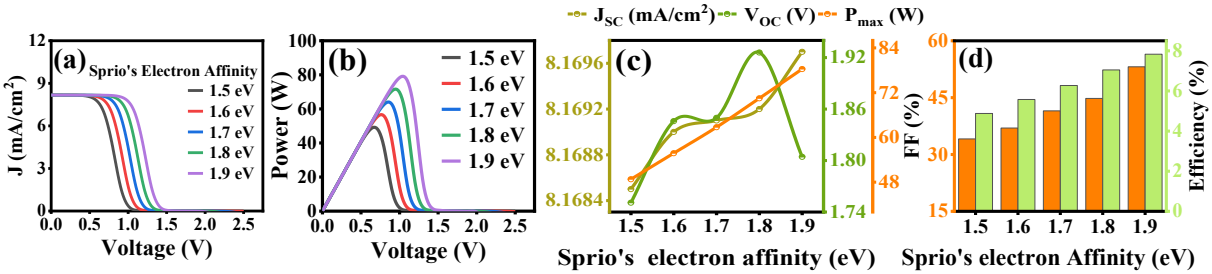

Figure 10(a) J-V curve, **(b)** P-V curve of TiO_2/BFO/Spiro-OMeTAD solar cell and effect of Spiro's electron affinity on **(c)** J_{sc}, V_{oc}, P_{max}, and **(d)** %FF and %efficiency (2-column fitting image).

Table 9 Designed device 1D (TiO_2/BFO/spiro-OMeTAD) performance parameters with varying Spiro's electron affinity

Spiro's affinity (eV)	J_{sc} (mA/cm^2)	V_{oc} (V)	P_{max} (W)	FF (%)	Efficiency (%)
1.5	8.168	1.750	48.789	34.113	4.878
1.6	8.169	1.845	55.760	36.978	5.576
1.7	8.169	1.849	62.733	41.514	6.273
1.8	8.169	1.925	70.483	44.799	7.048
1.9	8.169	1.804	78.326	53.136	7.832

4.9 Effect of operating temperature on PV performance

The operating temperature of a solar cell significantly influences its performance, primarily by intensifying phonon vibrations, which, in turn, increase internal resistances, such as the cell's series resistance. Elevated temperatures also raise the likelihood of collisions between charge

View Article Online
DOI: 10.1039/D5MA01257K

carriers and lattice ions, thereby amplifying recombination losses. Fig. 11(a) shows that if the temperature of device increases, it increases the random motion of charge carriers inside the layers of solar cells, and at low temperature their random motion is slower, as shown in Fig. 11(b).

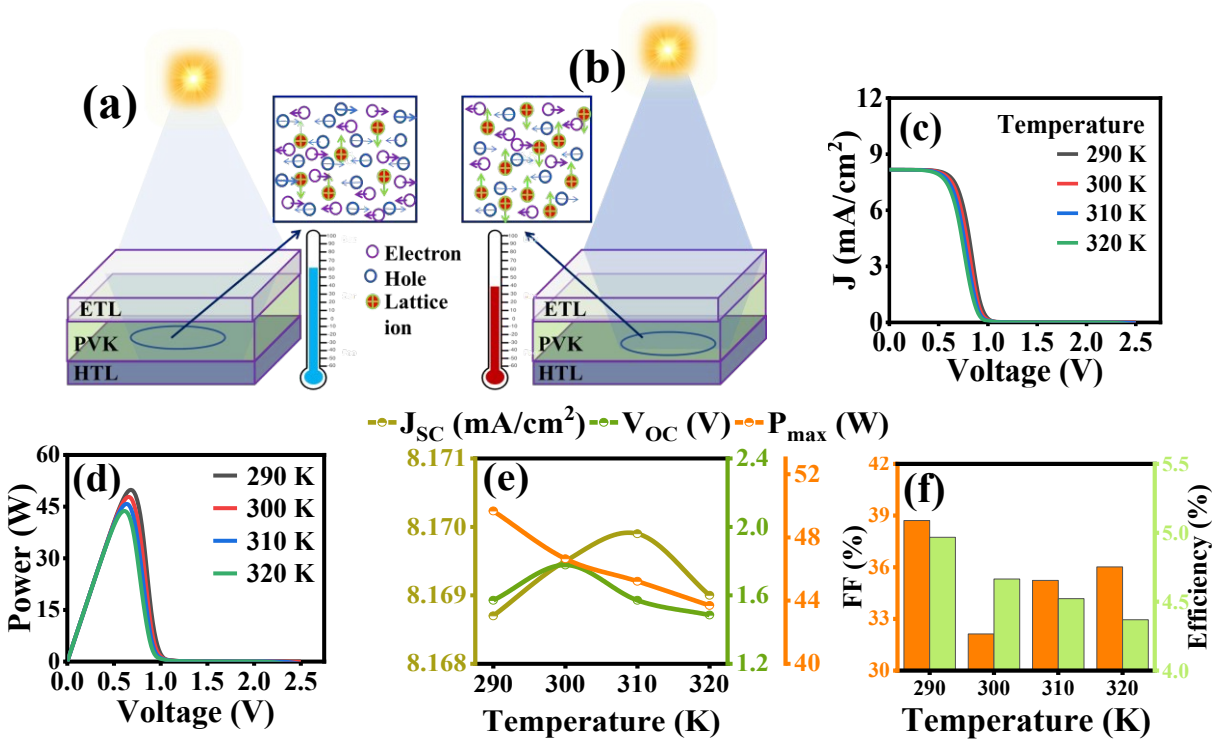

Figure 11(a) Higher temperature, **(b)** lower temperature effect on device internal environment, **(c)** J-V curve, **(d)** P-V curve of TiO_2/BFO/Spiro-OMeTAD solar cell and effect of temperature on **(e)** J_{sc}, V_{oc}, P_{max}, and **(f)** %FF and %efficiency (2-column fitting image).

Furthermore, Fig. 11(c,d) shows the J-V and P-V characteristics at different operating temperature values, ranging from 290 to 310 K, for the determination of J_{sc}, V_{oc}, and P_{max} of solar cell. Both J and P shows a very slight decline with temperature but sharply decreased at the V of 0.6 V. In Fig. 11(e), the J_{sc} exhibits minimal variation with temperature changes, although a slight decrease is observed at higher temperatures. Similarly, V_{oc} reduces from 1.57 to 1.48 V as temperature increases from 290 to 310 K, and this decline is attributed to bandgap narrowing and an increase in reverse saturation current, both of which negatively impact the device's ability to maintain a high V_{oc} at elevated temperatures. Moreover, P_{max} declines from 49.67 to 43.69 W, due to diminished FE polarization and increased recombination losses at higher temperatures, which collectively limit the charge extraction efficiency. However, FF initially decreases and then increases to 36.01% as temperature increases from 290 to 295 K, stabilizing thereafter as shown

View Article Online
DOI: 10.1039/D5MA01257K

in Fig. 11(f). This transient improvement is linked to enhanced carrier mobility and reduced series resistance, which temporarily offset the adverse effects of higher recombination rates. The η of solar cell slightly decreases from 4.96 to 4.36% with increasing temperature as shown in Fig. 11(f), attributable to the intrinsic narrow bandgap properties and moderate FE behavior of the PVK material, which mitigate significant performance degradation under thermal variations [83]. Finally, all the output characteristics with variation in operating device's temperature, are tabulated in Table 10.

Table 10 Designed device 1D (TiO_2/BFO/spiro-OMeTAD) performance parameters with varying operating temperature

Temperature (K)	J_{sc} (mA/cm^2)	V_{oc} (V)	P_{max} (W)	FF (%)	Efficiency (%)
290	8.1687	1.5709	49.674	38.711	4.967
300	8.1695	1.7772	46.644	32.126	4.664
310	8.1699	1.5709	45.221	35.235	4.522
320	8.1690	1.4849	43.690	36.017	4.369

4.10 Effect of SnS'thickness on PV performance of TiO_2/SnS/BFO/Spiro-OMeTAD solar cell

Fig. 12(a) shows the J-V characteristics of the TiO_2/SnS/BFO/Spiro-OMeTAD solar cell for different SnS absorber thicknesses. The J_{sc} increases with thickness due to enhanced photon absorption and efficient charge generation. However, at higher thickness, a noticeable voltage drop occurs near the open-circuit region, indicating increased recombination and reduced carrier collection efficiency in the thicker absorber layer. Fig. 12(b) presents the P-V characteristics for varying SnS absorber thicknesses. The output power increases with thickness up to 700 nm, indicating enhanced light absorption and efficient charge carrier extraction that result in higher P_{max}. However, at 1000 nm, a noticeable voltage drop occurs near the maximum power region, leading to a decline in power output. This reduction is primarily due to increased series resistance, longer carrier transport paths, and enhanced recombination in the thicker absorber layer, which collectively lower the overall conversion efficiency. Fig. 12(c) shows the variation of J_{sc}, V_{oc}, and P_{max} with different SnS thicknesses. The J_{sc} increases steadily from 31.02 to 31.98 mA/cm^2 as the thickness rises from 100 nm to 700 nm, which is attributed to enhanced optical absorption and a

View Article Online
DOI: 10.1039/D5MA01257K

higher generation rate of charge carriers within the active region. However, at 1000 nm, J_{sc} slightly drops to 31.45 mA/cm^2 due to enhanced bulk recombination and limited carrier diffusion in the thicker layer. The V_{oc} remains nearly constant around 0.80-0.81 V throughout the thickness range, showing that it is primarily governed by the built-in potential and interface quality rather than absorber thickness. The P_{max} follows a similar trend to J_{sc}, increasing from 196.16 to 209.95 W up to 700 nm, indicating efficient charge extraction and minimal resistive losses. Beyond this point, it decreases to 155.68 W at 1000 nm because of the increased series resistance and recombination effects, which reduce the overall power conversion capability.

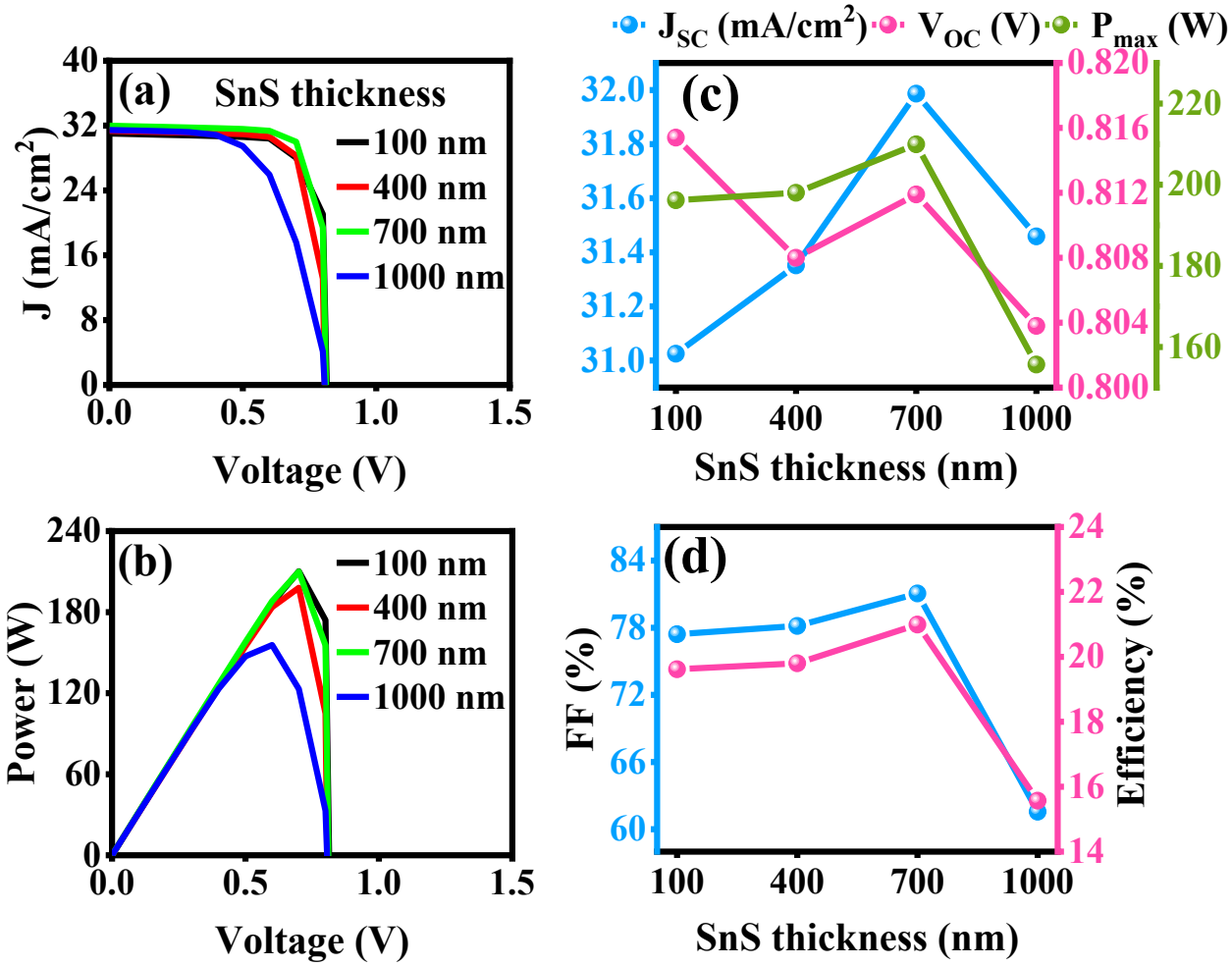

Figure 12(a) J-V curve, **(b)** P-V curve of TiO_2/SnS/BFO/Spiro-OMeTAD solar cell and effect of SnS' thickness on **(c)** J_{sc}, V_{oc}, P_{max}, and **(d)** %FF and %efficiency (2-column fitting image).

Fig. 12(d) illustrates the variation of FF and η with SnS absorber thickness. Both parameters show a gradual improvement as the thickness increases from 100 nm to 700 nm, where

View Article Online
DOI: 10.1039/D5MA01257K

the FF rises from 77.41% to 81.06% and the efficiency reaches its peak value of 20.99%. This enhancement is attributed to improved light absorption, efficient charge separation, and reduced recombination within the optimal thickness range. However, at 1000 nm, the FF drops sharply to 61.56% and the efficiency decreases to 15.56%, mainly due to higher series resistance, enhanced recombination losses, and limited carrier diffusion in the overly thick absorber layer. These results confirm that 700 nm is the optimum SnS thickness for achieving maximum device performance.

5 Conclusion

Global warming and the reliance on hazardous energy sources have intensified the search for environment friendly energy alternative. Among these, solar energy has emerged as a cost-effective, sustainable, and clean solution to meet the rising energy demands of the world's growing population. For decades, researchers have been exploring suitable materials to enhance the stability, cost-efficiency, and performance of solar cells. In this context, perovskite materials, particularly $BiFeO_3$, have gained significant attention as absorber layers due to their multifunctional properties, including room-temperature ferroelectricity and strong permanent polarization, which eliminate the need for conventional p-n junctions. This study employs COMSOL simulation software to model 1D TiO_2/$BiFeO_3$/Spiro-OMeTAD and 1D TiO_2/SnS/$BiFeO_3$/Spiro-OMeTAD solar cell configurations, assuming ideal ohmic front and back metal contacts. Key parameters such as the thickness and electron affinities of $BiFeO_3$, TiO_2, and Spiro-OMeTAD layers, as well as the density of states in the valence and conduction bands of $BiFeO_3$ and TiO_2, and operating temperature, were systematically varies to evaluate their impact on the cell's photovoltaic performance. The results demonstrate that short-circuit current density increases linearly (from 3.697 to 9.004 mA/cm^2) with $BiFeO_3$ thickness (from 50 to 1850 nm), and efficiency reaches a maximum (10.101%) at an optimal thickness (nearly 600 nm). However, efficiency decreases (from 4.881 to 4.876%) with increased TiO_2 thickness (from 10 to 150 nm), while power output and efficiency steadily rise (ranging 101-103.45 W & 10.15-10.35%) with the thickness of the hole transport layer (ranging 10-150 nm). For SnS layer's thickness, at 700 nm the device showed maximum efficiency of 20.99% in TiO_2/SnS/$BiFeO_3$/Spiro-OMeTAD configuration. The density of states in BFO has a decreasing impact on efficiency and reduces open-circuit voltage (from 1.99 to 1.235 V) confirming the inverse relation between them, while an increase in the density of states in ETL leads to increase in efficiency (from 6.08 to 10.88%). Additionally, increasing the electron affinity of $BiFeO_3$ (from 3.3 to 3.5 eV) decreases the fill

View Article Online
DOI: 10.1039/D5MA01257K

factor (from 52.987 to 35.411%), while increasing the electron affinity of TiO_2 (3.5 to 3.7 eV) enhances the open-circuit voltage (1.49 to 1.63 V), and that of Spiro improves the power output (48.78 to 78.32 W). However, a rise in the device's operating temperature (from 290 to 310 K) reduces overall efficiency (from 4.96 to 4.36%) of solar cell. This study aids for optimizing material properties and device parameters for experimental purposes and encourages the potential of $BiFeO_3$-based perovskite materials as potential candidates for next-generation photovoltaic applications.

Data Availability Statement:

Data will be made available on request.

Conflict of Interest:

The authors declare that there are no financial or any other types of conflicts of interests to declare for this submission.

References

[1] Ajayan, J., Nirmal, D., Mohankumar, P., Saravanan, M., Jagadesh, M., & Arivazhagan, L. (2020). A review of photovoltaic performance of organic/inorganic solar cells for future renewable and sustainable energy technologies. *Superlattices and Microstructures*, *143*, 106549.

[2] Al-Shahri, O. A., Ismail, F. B., Hannan, M. A., Lipu, M. H., Al-Shetwi, A. Q., Begum, R. A., Al-Muhsen, N.F., & Soujeri, E. (2021). Solar photovoltaic energy optimization methods, challenges and issues: A comprehensive review. *Journal of Cleaner Production*, *284*, 125465.

[3] Singh, B. P., Goyal, S. K., & Kumar, P. (2021). Solar PV cell materials and technologies: Analyzing the recent developments. *Materials Today: Proceedings*, *43*, 2843-2849.

[4] Sahoo, P., Tiwari, C., Kukreti, S., & Dixit, A. (2024). All oxide lead-free bismuth ferrite perovskite absorber based FTO/ZnO/$BiFeO_3$/Au solar cell with efficiency~ 12%: First principle material and macroscopic device simulation studies. *Journal of Alloys and Compounds*, *981*, 173599.

View Article Online
DOI: 10.1039/D5MA01257K

[5] Chen, J., Dong, H., Li, J., Zhu, X., Xu, J., Pan, F., Xu, R., Xi, J., Jiao, B., Hou, X., & Wu, Z. (2022). Solar cell efficiency exceeding 25% through Rb-based perovskitoid scaffold stabilizing the buried perovskite surface. *ACS Energy Letters*, *7*(10), 3685-3694.

[6] Zhang, J., Li, X., Wang, L., Yu, J., Wageh, S., & Al-Ghamdi, A. A. (2021). Enhanced performance of $CH_3NH_3PbI_3$ perovskite solar cells by excess halide modification. *Applied Surface Science*, *564*, 150464.

[7] Wang, R., Mujahid, M., Duan, Y., Wang, Z. K., Xue, J., & Yang, Y. (2019). A review of perovskites solar cell stability. *Advanced Functional Materials*, *29*(47), 1808843.

[8] Seyfouri, M. M., & Wang, D. (2021). Recent progress in bismuth ferrite-based thin films as a promising photovoltaic material. *Critical Reviews in Solid State and Materials Sciences*, *46*(2), 83-108.

[9] Han, X., Ji, Y., & Yang, Y. (2022). Ferroelectric photovoltaic materials and devices. *Advanced Functional Materials*, *32*(14), 2109625.

[10] Taheri-Ledari, R., Ganjali, F., Zarei-Shokat, S., Saeidirad, M., Ansari, F., Forouzandeh-Malati, M., Hassanzadeh-Afruzi, F., Hashemi, S.M., & Maleki, A. (2022). A review of metal-free organic halide perovskite: future directions for the next generation of solar cells. *Energy & Fuels*, *36*(18), 10702-10720.

[11] Li, H., Li, F., Shen, Z., Han, S. T., Chen, J., Dong, C., & Wang, M. (2021). Photoferroelectric perovskite solar cells: Principles, advances and insights. *Nano Today*, *37*, 101062.

[12] Li, D. F., Deng, X. H., Ma, Y. X., Liu, D. S., Huang, X. F., Zhao, X. F., Chen, W.T., & Sui, Y. (2021). A near-room-temperature hybrid organic–inorganic lead halide perovskite ferroelectric $[BrCH_2CH_2N(CH_3)_3][PbBr_3]$ and its flexible composite film. *The Journal of Physical Chemistry C*, *126*(1), 728-736.

[13] Sun, Z., Wei, J., Song, S., Xiahou, M., Cao, A., Zhang, J., Yuanfeng, Y., Chen, G., & Chen, Y. (2024). Multiple strategies to greatly enhance the photovoltaic characteristics of $BiFeO_3$-based films. *Inorganic Chemistry Frontiers*, *11*(15), 4780-4793.

[14] Chen, G., Chen, J., Pei, W., Lu, Y., Zhang, Q., Zhang, Q., & He, Y. (2019). Bismuth ferrite materials for solar cells: current status and prospects. *Materials Research Bulletin*, *110*, 39-49.

View Article Online
DOI: 10.1039/D5MA01257K

[15] Abdelsamie, A., You, L., Wang, L., Li, S., Gu, M., & Wang, J. (2022). Crossover between bulk and interface photovoltaic mechanisms in a ferroelectric vertical heterostructure. *Physical Review Applied*, *17*(2), 024047.

[16] Jiang, Y. P., Zhou, H. C., Tang, X. G., Li, W. H., Guo, X. B., Tang, Z. H., & Liu, Q. X. (2023). Enhanced and controllable ferroelectric photovoltaic effects in $Bi_4Ti_3O_{12}/TiO_2$ composite films. *Journal of Electronic Materials*, *52*(1), 188-195.

[17] Das, S., Ghara, S., Mahadevan, P., Sundaresan, A., Gopalakrishnan, J., & Sarma, D. D. (2018). Designing a lower band gap bulk ferroelectric material with a sizable polarization at room temperature. *ACS Energy Letters*, *3*(5), 1176-1182.

[18] Salman, M. U., Waqas, U., Quader, A., Ramay, S. M., Rehman, M. O. U., & Atiq, S. (2024). Concurrent existence of magneto-electric coupling and electro-optic Kerr effect in perovskite-based ternary composites for energy reservoirs. *Journal of Alloys and Compounds*, *976*, 173217.

[19] Gradauskaite, E., Meisenheimer, P., Müller, M., Heron, J., & Trassin, M. (2021). Multiferroic heterostructures for spintronics. *Physical Sciences Reviews*, *6*(2), 20190072.

[20] Taniyama, T., Gohda, Y., Hamaya, K., & Kimura, T. (2024). Artificial multiferroic heterostructures—electric field effects and their perspectives. *Science and Technology of Advanced Materials*, *25*(1), 2412970.

[21] Zhang, J. W., Deng, W., Ye, Z., Diaham, S., Putson, C., Zhou, X., Hu, J., Yin, Z., & Jia, R. (2023). Aging phenomena of backsheet materials of photovoltaic systems for future zero-carbon energy and the improvement pathway. *Journal of Materials Science & Technology*, *153*, 106-119.

[22] Liu, Y., Wang, Y., Ma, J., Li, S., Pan, H., Nan, C. W., & Lin, Y. H. (2022). Controllable electrical, magnetoelectric and optical properties of $BiFeO_3$ via domain engineering. *Progress in Materials Science*, *127*, 100943.

[23] Li, Z., Zhao, Y., Li, W. L., Song, R., Zhao, W., Wang, Z., Peng, Y., & Fei, W. D. (2021). Photovoltaic effect induced by self-polarization in $BiFeO_3$ films. *The Journal of Physical Chemistry C*, *125*(17), 9411-9418.

View Article Online
DOI: 10.1039/D5MA01257K

[24] Valsalakumar, S., Roy, A., Mallick, T. K., Hinshelwood, J., & Sundaram, S. (2022). An Overview of Current Printing Technologies for Large-Scale Perovskite Solar Cell Development. *Energies*, *16*(1), 190.

[25] Akel, S., Kulkarni, A., Rau, U., & Kirchartz, T. (2023). Relevance of long diffusion lengths for efficient halide perovskite solar cells. *PRX Energy*, *2*(1), 013004.

[26] Raj, A., Kumar, M., Kumar, A., Singh, K., Sharma, S., Singh, R. C., Pawar, M.S., Yahya, M.Z.A., & Anshul, A. (2023). Comparative analysis of 'La'modified $BiFeO_3$-based perovskite solar cell devices for high conversion efficiency. *Ceramics International*, *49*(1), 1317-1327.

[27] Misiurev, D., Kaspar, P., & Holcman, V. (2022). Brief theoretical overview of Bi-Fe-O based thin films. *Materials*, *15*(24), 8719.

[28] Martínez, A. B., Grysan, P., Girod, S., Glinsek, S., & Granzow, T. (2022). Direct evidence for bulk photovoltaic charge transport in a ferroelectric polycrystalline film. *Scripta Materialia*, *211*, 114498.

[29] Teuschel, M., Heyes, P., Horvath, S., Novotny, C., & Rusconi Clerici, A. (2022). Temperature stable piezoelectric imprint of epitaxial grown PZT for zero-bias driving MEMS actuator operation. *Micromachines*, *13*(10), 1705.

[30] Liang, K. Y., Wang, Y. F., Yang, Z., Zhang, S. P., Jia, S. Y., & Zeng, J. H. (2021). Above-band-gap voltage from oriented bismuth ferrite ceramic photovoltaic cells. *ACS Applied Energy Materials*, *4*(11), 12703-12708.

[31] Gholizadeh, A., & Hosseini, S. (2024). Effect of heavy rare-earth substitution on physical properties of $BiFeO_3$ thin films and their photocatalytic application. *Journal of the American Ceramic Society*, *107*(6), 4209-4222.

[32] Mana-ay, H., Chen, C. S., Chien, R. R., Tu, C. S., & Chen, P. Y. (2024). Achieving high microscale photoconductivity in Gd-modified bismuth ferrite via modulating ferroelectric polarization. *Journal of Materials Chemistry C*, *12*(30), 11529-11539.

[33] Lin, J., Chen, Y., Wang, H., Tian, B., Chen, Y., Zhou, Z., Yue, F., Huang, R., Duan, C.G., Chu, J., & Sun, L. (2023). Unveiling the Anomalous Photovoltaic Effect of Ferroelectric Domain Walls in $BiFeO_3$ Thin Films. *Physical Review Applied*, *19*(2), 024050.

View Article Online
DOI: 10.1039/D5MA01257K

[34] Deng, J., Huang, B., Li, W., Zhang, L., Jeong, S. Y., Huang, S., Zhang, S., Wu, F., Xu, X., Zou, G., & Chen, L. (2022). Ferroelectric polymer drives performance enhancement of non-fullerene organic solar cells. *Angewandte Chemie International Edition*, *61*(25), e202202177.

[35] Singh, A., Prakash, C., Sahoo, P., & Dixit, A. (2024). $BiFeO_3$ perovskite-based all oxide ambient stable spectrally selective absorber coatings for solar thermal application. *Sustainable Energy & Fuels*, *8*(12), 2762-2776.

[36] Afzal, A. M., Javed, Y., Hussain, S., Ali, A., Yaqoob, M. Z., & Mumtaz, S. (2020). Enhancement in photovoltaic properties of bismuth ferrite/zinc oxide heterostructure solar cell device with graphene/indium tin oxide hybrid electrodes. *Ceramics International*, *46*(7), 9161-9169.

[37] Tuluk, A., Brouwer, H., & van der Zwaag, S. (2022). Controlling the Oxygen Defects Concentration in a Pure $BiFeO_3$ Bulk Ceramic. *Materials*, *15*(19), 6509.

[38] Gumiel, C., & Calatayud, D. G. (2022). Thin film processing of multiferroic $BiFeO_3$: From sophistication to simplicity. A review. *Boletín de la Sociedad Española de Cerámica y Vidrio*, *61*(6), 708-732.

[39] Spaldin, N. A., Efe, I., Rossell, M. D., & Gattinoni, C. (2021). Layer and spontaneous polarizations in perovskite oxides and their interplay in multiferroic bismuth ferrite. *The Journal of Chemical Physics*, *154*(15).

[40] Wang, C., Song, Y., Wu, L., Xue, C., Feng, H., Li, H., Song, J., Zhang, X., Zou, B., & Zhu, K. (2024). Structure and ferroelectric photovoltaic effect modulation in the epitaxial $BiFeO_3/La_{0.5}Sr_{0.5}CO_3$ heterostructures. *Micro and Nanostructures*, *195*, 207956.

[41] Chelil, N., Sahnoun, M., Benhalima, Z., Larbi, R., & Eldin, S. M. (2023). Insights into the relationship between ferroelectric and photovoltaic properties in $CsGeI_3$ for solar energy conversion. *RSC Advances*, *13*(3), 1955-1963.

[42] Pei, W., Chen, J., You, D., Zhang, Q., Li, M., Lu, Y., Fu, Z., & He, Y. (2020). Enhanced photovoltaic effect in Ca and Mn co-doped $BiFeO_3$ epitaxial thin films. *Applied Surface Science*, *530*, 147194.

View Article Online
DOI: 10.1039/D5MA01257K

[43] Ray, A., Basu, T., Behera, B., Kumar, M., Thapa, R., & Nayak, P. (2018). Role of Gd-doping in conduction mechanism of BFO-PZO nanocrystalline composites: experimental and first-principles studies. *Journal of Alloys and Compounds*, *768*, 198-213.

[44] Gupta, R., Singh, S. P., Walia, R., Kumar, V., & Verma, V. (2022). Modification in photovoltaic and photocatalytic properties of bismuth ferrites by tailoring band-gap and ferroelectric properties. *Journal of Alloys and Compounds*, *908*, 164602.

[45] Yin, X., Chen, C., Fan, Z., Qin, M., Zeng, M., Lu, X., Zhou, G., Gao, X., Chen, D., & Liu, J. M. (2021). Coexistence of multiple morphotropic phase boundaries in strained La-doped $BiFeO_3$ thin films. *Materials Today Physics*, *17*, 100345.

[46] Dhanalakshmi, R., Giridharan, N. V., & Denardin, J. C. (2021). Magnetic Field-Assisted Photocatalytic Degradation of Organic Pollutants over $Bi_{1-x}R_xFeO_3$ (R= Ce, Tb; x= 0.00, 0.05, 0.10 and 0.15) Nanostructures. *Materials*, *14*(15), 4079.

[47] Čebela, M., Zagorac, D., Popov, I., Torić, F., Klaser, T., Skoko, Ž., & Pajić, D. (2023). Enhancement of weak ferromagnetism, exotic structure prediction and diverse electronic properties in holmium substituted multiferroic bismuth ferrite. *Physical Chemistry Chemical Physics*, *25*(33), 22345-22358.

[48] Tian, C., Yao, Q., Tong, Z., Rao, G., Deng, J., Wang, Z., Wang, J., Zhou, H., & Zhao, J. (2021). The influence of Nd substitution on microstructural, magnetic, and microwave absorption properties of $BiFeO_3$ nanopowders. *Journal of Alloys and Compounds*, *859*, 157757.

[49] Khan, M., Iqbal, M. A., Malik, M., Hashmi, S. U. M., Bakhsh, S., Sohail, M., Qamar, M.T., Al-Bahrani, M., Capangpangan, R.Y., Alguno, A.C., & Choi, J. R. (2023). Improving the efficiency of dye-sensitized solar cells based on rare-earth metal modified bismuth ferrites. *Scientific Reports*, *13*(1), 3123.

[50] Sunny, A., Rahman, S., Khatun, M., & Ahmed, S. R. A. (2021). Numerical study of high performance HTL-free $CH_3NH_3SnI_3$-based perovskite solar cell by SCAPS-1D. *AIP Advances*, *11*(6), 065102.

View Article Online
DOI: 10.1039/D5MA01257K

[51] Tractz, G. T., Antunes, S. R. M., & Rodrigues, P. R. P. (2023). Nb/TiO_2 oxides: A study of synthesis and electron transport mechanism as an ETL in a solar device. *Journal of Photochemistry and Photobiology A: Chemistry*, *444*, 114899.

[52] Kim, J. Y., Lee, J. W., Jung, H. S., Shin, H., & Park, N. G. (2020). High-efficiency perovskite solar cells. *Chemical Reviews*, *120*(15), 7867-7918.

[53] Kumar, N. S., & Naidu, K. C. B. (2021). A review on perovskite solar cells (PSCs), materials and applications. *Journal of Materiomics*, *7*(5), 940-956.

[54] Hossain, M. K., Samajdar, D. P., Das, R. C., Arnab, A. A., Rahman, M. F., Rubel, M. H. K., & Mohammed, M. K. (2023). Design and simulation of Cs_2BiAgI_6 double perovskite solar cells with different electron transport layers for efficiency enhancement. *Energy & Fuels*, *37*(5), 3957-3979.

[55] Sebastian, V., & Kurian, J. (2021). Simulation and optimization studies on $CsPbI_3$ based inorganic perovskite solar cells. *Solar Energy*, *221*, 99-108.

[56] Singh, A. K., Srivastava, S., Mahapatra, A., Baral, J. K., & Pradhan, B. (2021). Performance optimization of lead free-$MASnI_3$ based solar cell with 27% efficiency by numerical simulation. *Optical Materials*, *117*, 111193.

[57] De Los Santos, I. M., Cortina-Marrero, H. J., Ruíz-Sánchez, M. A., Hechavarría-Difur, L., Sánchez-Rodríguez, F. J., Courel, M., & Hu, H. (2020). Optimization of $CH_3NH_3PbI_3$ perovskite solar cells: A theoretical and experimental study. *Solar Energy*, *199*, 198-205.

[58] Karthick, S., Velumani, S., & Bouclé, J. (2020). Experimental and SCAPS simulated formamidinium perovskite solar cells: A comparison of device performance. *Solar Energy*, *205*, 349-357.

[59] Carlini, M., McCormack, S. J., Castellucci, S., Ortega, A., Rotondo, M., & Mennuni, A. (2020). Modelling and numerical simulation for an innovative compound solar concentrator: Thermal analysis by FEM approach. *Energies*, *13*(3), 548.

[60] Zandi, S., Saxena, P., Razaghi, M., & Gorji, N. E. (2020). Simulation of CZTSSe thin-film solar cells in COMSOL: Three-dimensional optical, electrical, and thermal models. *IEEE Journal of Photovoltaics*, *10*(5), 1503-1507.

View Article Online
DOI: 10.1039/D5MA01257K

[61] Dehghani, N., Jamekhorshid, A., Jalali, T., & Osfouri, S. (2024). Numerical modeling of charge transfer and recombination kinetics in the dye-sensitized solar cell: Conceptual integration of optics, electricity, and electrochemistry. *Renewable Energy*, *239*, 122150.

[62] Abdel, D., Glitzky, A., & Liero, M. (2025). Analysis of a drift-diffusion model for perovskite solar cells. *Discrete and Continuous Dynamical Systems-B*, *30*(1), 99-131.

[63] Clarke, W., Wolf, M. J., Walker, A., & Richardson, G. (2023). Charge transport modelling of perovskite solar cells accounting for non-Boltzmann statistics in organic and highly-doped transport layers. *Journal of Physics: Energy*, *5*(2), 025007.

[64] Shah, D. K., Devendra, K. C., Muddassir, M., Akhtar, M. S., Kim, C. Y., & Yang, O. B. (2021). A simulation approach for investigating the performances of cadmium telluride solar cells using doping concentrations, carrier lifetimes, thickness of layers, and band gaps. *Solar Energy*, *216*, 259-265.

[65] Song, T., Friedman, D. J., & Kopidakis, N. (2021). Comprehensive performance calibration guidance for perovskites and other emerging solar cells. *Advanced Energy Materials*, *11*(23), 2100728.

[66] Karmani, Y. K., Bilal, M., Salman, M. U., Ameen, M., Luqman, M., Ramay, S. M., Younis, M. & Atiq, S. (2025). Correlation between trap-assisted non-radiative recombination losses and thermal agitation in SnS-based solar cell: A state-of-the-art computational analysis. *Materials Science and Engineering: B*, *321*, 118484.

[67] Kumar, M., Pundir, S. K., & Singh, D. V. (2024). Effect on green energy conversion and stability with 'Er'modification in multiferroic based perovskite solar cell devices. *Materials Today Communications*, *38*, 107841.

[68] Li, Y., Wei, J., Sun, Z., Yang, T., Liu, Z., Chen, G., Zhao, L., & Cheng, Z. (2022). Greatly enhanced photocurrent density in bismuth ferrite films by Localized Surface Plasmon Resonance effect. *Applied Surface Science*, *583*, 152571.

[69] Nakamura, T., Yanwachirakul, W., Imaizumi, M., Sugiyama, M., Akiyama, H., & Okada, Y. (2021). Reducing Shockley–Read–Hall recombination losses in the depletion region of a solar cell by using a wide-gap emitter layer. *Journal of Applied Physics*, *130*(15), 153102.

View Article Online
DOI: 10.1039/D5MA01257K

[70] Fatima, Q., Haidry, A. A., Zhang, H., El Jery, A., & Aldrdery, M. (2024). A critical review on advancement and challenges in using TiO_2 as electron transport layer for perovskite solar cell. *Materials Today Sustainability*, *27*, 100857.

[71] Dabas, S., Kumar, M., Singh, D. V., & Kumar, P. (2024). Cutting-edge technologies and recent modernization on multifunctional perovskite materials for green energy conversion and spintronic applications. *Materials Letters*, *377*, 137389.

[72] Tumen-Ulzii, G., Matsushima, T., & Adachi, C. (2021). Mini-review on efficiency and stability of perovskite solar cells with Spiro-OMeTAD hole transport layer: Recent progress and perspectives. *Energy & Fuels*, *35*(23), 18915-18927.

[73] Ait-Wahmane, Y., Mouhib, H., Ydir, B., Ait Hssi, A., Atourki, L., Ihlal, A., & Bouabid, K. (2022). Comparison study between ZnO and TiO_2 in CuO based solar cell using SCAPS-1D. *Materials Today: Proceedings*, *52*, 166-171.

[74] Salman, M. U., Bilal, M., Karmani, Y. K., Ali, U., Ramay, S. M., Younis, M., & Atiq, S. (2025). Influence of acceptor/donor densities and layer thicknesses on the efficiency of 2D ZnO/BFO/spiro-OMeTAD perovskite solar cells: a COMSOL simulation-based optimization. *Journal of Materials Chemistry A*, *13*(20), 15057-15066.

[75] Mudassar, M. M., Arshad, M., Salman, M. U., Mahmood, A., Al-Masry, W., Asim, M., & Atiq, S. (2025). Significance of the direct relation between the fill factor and hole transport layer thickness in perovskite-based solar cells for green energies. *RSC Advances*, *15*(40), 33830-33843.

[76] Kumar, M., Singh, D. V., Sharma, S., Dwivedi, D. K., Anshul, A., Hossain, M. K., & Pundir, S. K. (2025). Investigations on interfacial complex dynamic processes of Er-$BiFeO_3$ based perovskite solar cell heterostructures. *Inorganic Chemistry Communications*, *171*, 113587.

[77] Mukametkali, T. M., Ilyassov, B. R., Aimukhanov, A. K., Serikov, T. M., Baltabekov, A. S., Aldasheva, L. S., & Zeinidenov, A. K. (2023). Effect of the TiO_2 electron transport layer thickness on charge transfer processes in perovskite solar cells. *Physica B: Condensed Matter*, *659*, 414784.

[78] Alam, I., & Ashraf, M. A. (2024). Effect of different device parameters on tin-based perovskite solar cell coupled with In_2S_3 electron transport layer and CuSCN and Spiro-OMeTAD alternative

View Article Online
DOI: 10.1039/D5MA01257K

hole transport layers for high-efficiency performance. *Energy Sources, Part A: Recovery, Utilization, and Environmental Effects*, *46*(1), 17080-17096.

[79] Dwivedi, D. K. (2020). Modeling of CZTSSe solar photovoltaic cell for window layer optimization. *Optik*, *222*, 165407.

[80] Jeyakumar, R., Bag, A., Nekovei, R., & Radhakrishnan, R. (2020). Influence of electron transport layer (TiO_2) thickness and its doping density on the performance of $CH_3NH_3PbI_3$-based planar perovskite solar cells. *Journal of Electronic Materials*, *49*(6), 3533-3539.

[81] Chen, H., Li, Z. Q., Sun, B., & Feng, X. D. (2021). Towards high-efficiency planar heterojunction antimony sulfide solar cells. *Optical Materials*, *121*, 111556.

[82] Rombach, F. M., Haque, S. A., & Macdonald, T. J. (2021). Lessons learned from spiro-OMeTAD and PTAA in perovskite solar cells. *Energy & Environmental Science*, *14*(10), 5161-5190.

[83] Garain, R., Basak, A., & Singh, U. P. (2021). Study of thickness and temperature dependence on the performance of SnS based solar cell by SCAPS-1D. *Materials Today: Proceedings*, *39*, 1833-1837.

View Article Online
DOI: 10.1039/D5MA01257K

Data Availability Statement

The data will be available on request.